Electronic Supplementary Material of

Spatial, Temporal, and Spectral Characterizations and Kinetic Investigations of a High Repetition-Rate Laser-Induced Micro-Plasma in Air

Yi You‡, Andreas Bierstedt‡, and Jens Riedel

Federal Institute for Materials Research and Testing (BAM), Richard-Willstätter-Strasse 11, 12489 Berlin, Germany

‡ The authors contributed equally to this work.

1. Assessment of image distortion

To evaluate the possible image distortion introduced by the optics, a wire mesh with square hole was aligned at the surface of plasma ignition. The image acquired showed the patterns of the wire mesh (*cf.* Figure S1). As such, we confirmed that the plasma images acquired with the setup were not distorted through the optics.

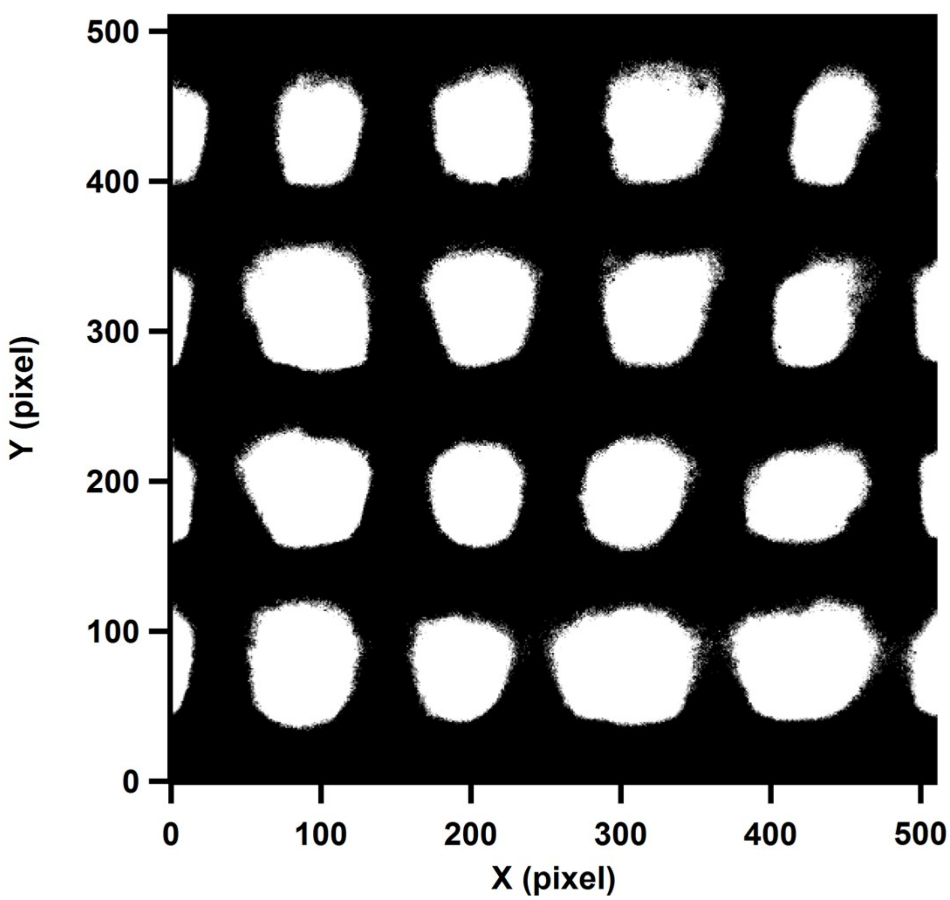

Figure S1. Image of a square wire mesh with the acquisition optics.

2. Determination of magnification factor

The magnification factor, in unit of μ/pixel, was measured with a standard needle with an outer diameter of 800 μm. An image of the needle with the acquisition optics was taken (*cf.* Figure S2). The edge detection was performed by first setting the threshold value of 1000 counts, which was arbitrarily chosen. A margin of 10% was used to filter the edge points thereafter (*cf.* Figure S2, black dots). To find the normal line between the edges, a modified linear regression algorithm was used. In particular, the slopes for the edge lines were constrained to be the same. The distance between the edges were found to be 401.93 pixel (*cf.* Figure S2, white arrow). As such, the magnification factor was 1.995 μm/pixel.

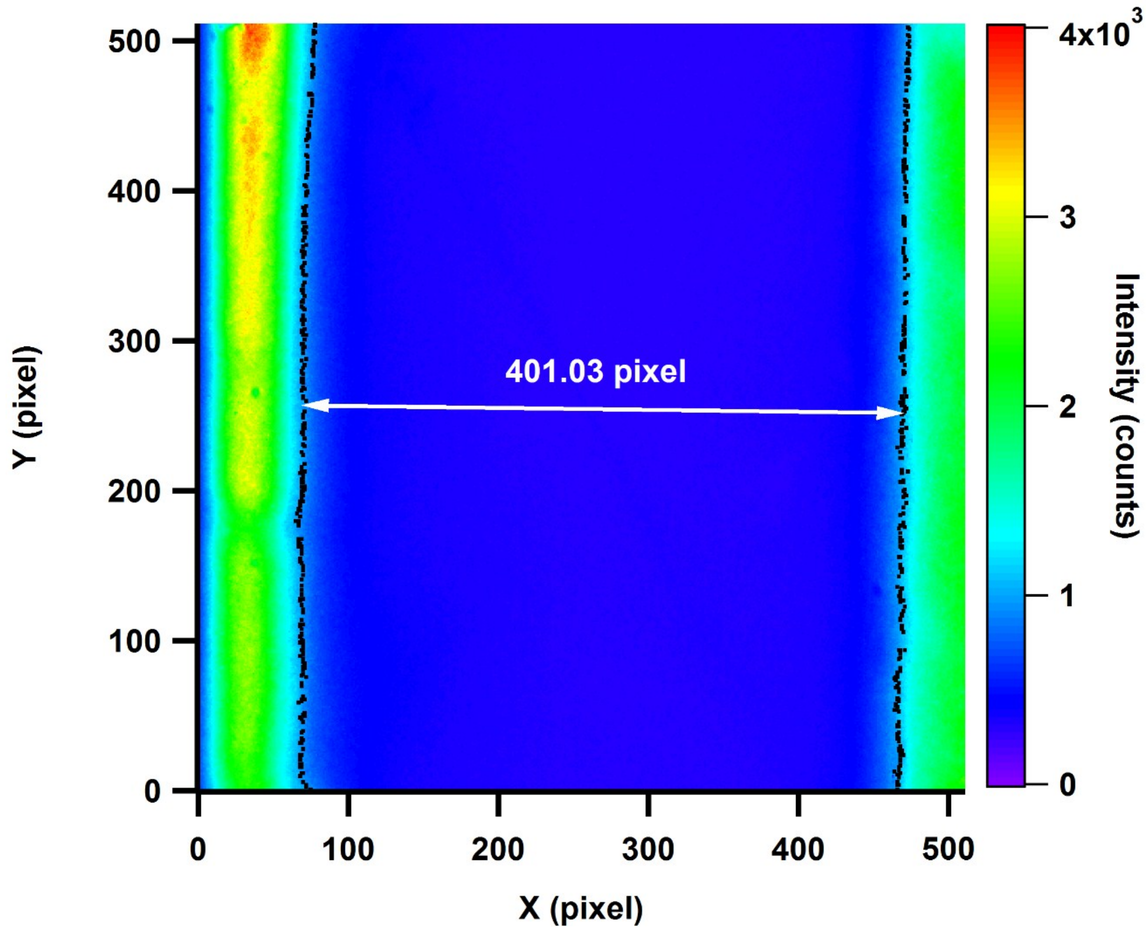

Figure S2. Image of a needle with an outer diameter of 800 μm. The black dots are the edges found at the threshold value. The white arrow is the pixel distance between the two edge lines.

3. Spatially integrated emission spectrum

In order to investigate the transient optical emission in a large spectral range, an Echelle spectrometer equipped with an iCCD (Butterfly, LTB GmbH, Berlin, Germany) was used. The photocathode was gated at 4 ns with a step size of 1 ns.

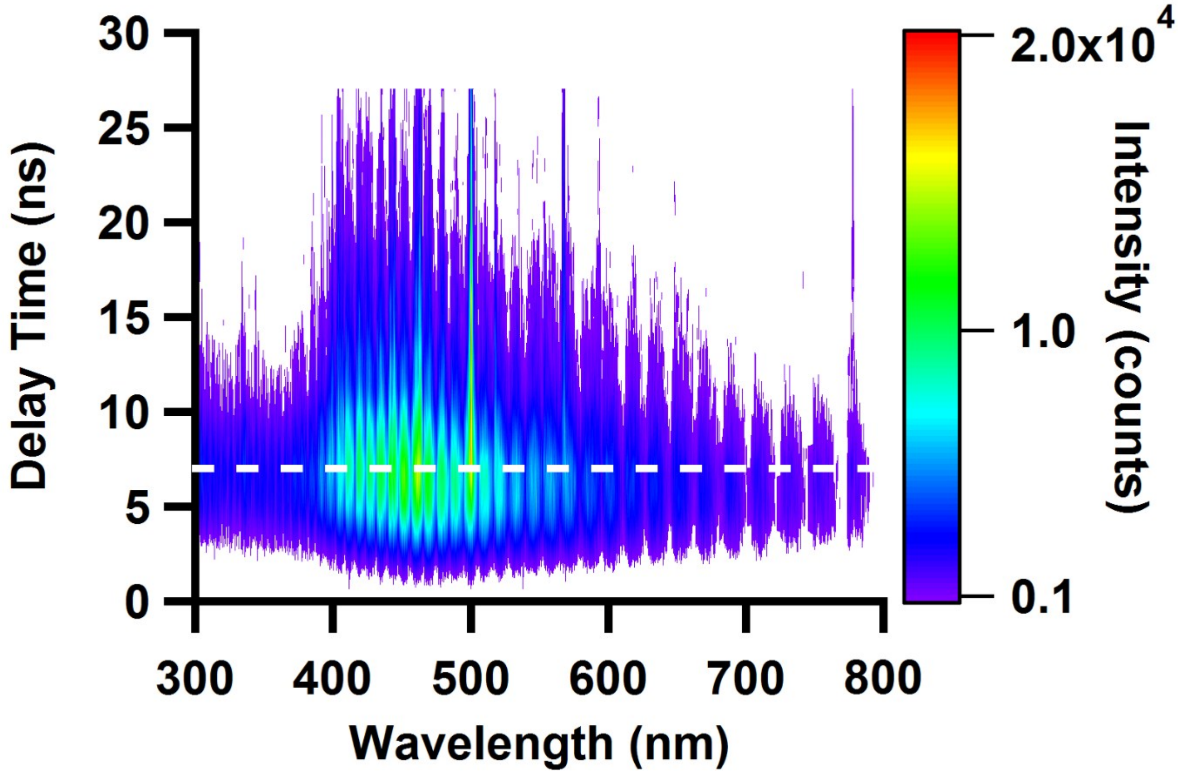

Figure S3. Temporally resolved, but spatially integrated optical emission spectrum of the airborne plasma.

4. Experimentally measured laser profile

The transient laser profile was measured with a fast-response photo-diode (DET210, Thorlabs, Dachau, Germany) directly connected to an oscilloscope (DL9140, 5 GS/s, 1 GHz, Yokogawa, Musashino, Japan). Several neutral density filters (Ne10a and NdUV10a, both Thorlabs, Dachau, Germany) were used in front of the detector to compensate the laser intensity. Additionally, the laser beam was splatted with a microscope slide to transfer ~4% of the laser towards the laser diode.

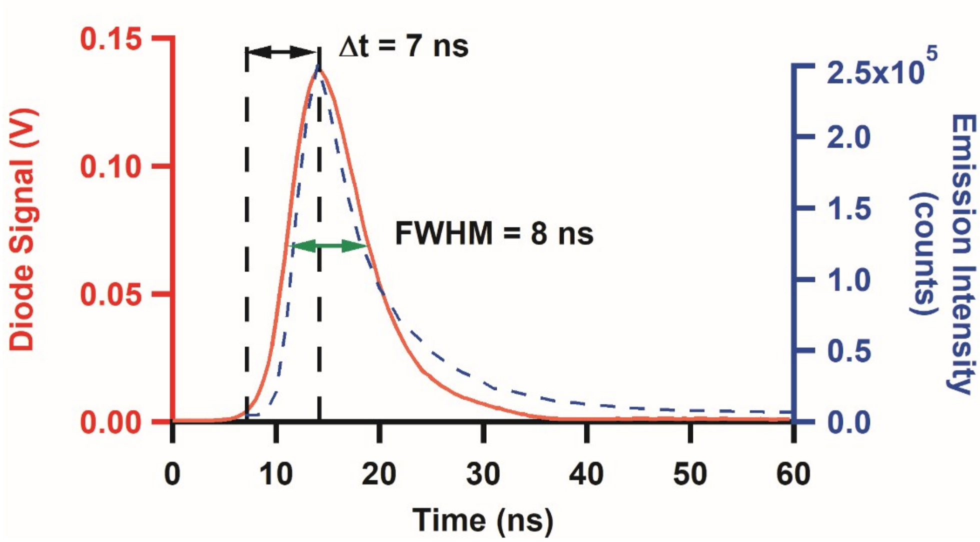

Figure S4. Transient laser profile. The red solid line and the dashed blue line represented the transient diode voltage for measuring the laser and the OES signal from the plasma center, respectively.

The photodiode and the spectrograph used in this study exhibited different time responses. Throughout this study, we did not perform any further investigation on the instrument responses function. In this case, to align the two transient profiles acquired in two different clock domains, the time points where maximal signals occurred for both cases were set as the common point.

5. Integrated temporal emission profiles of different species

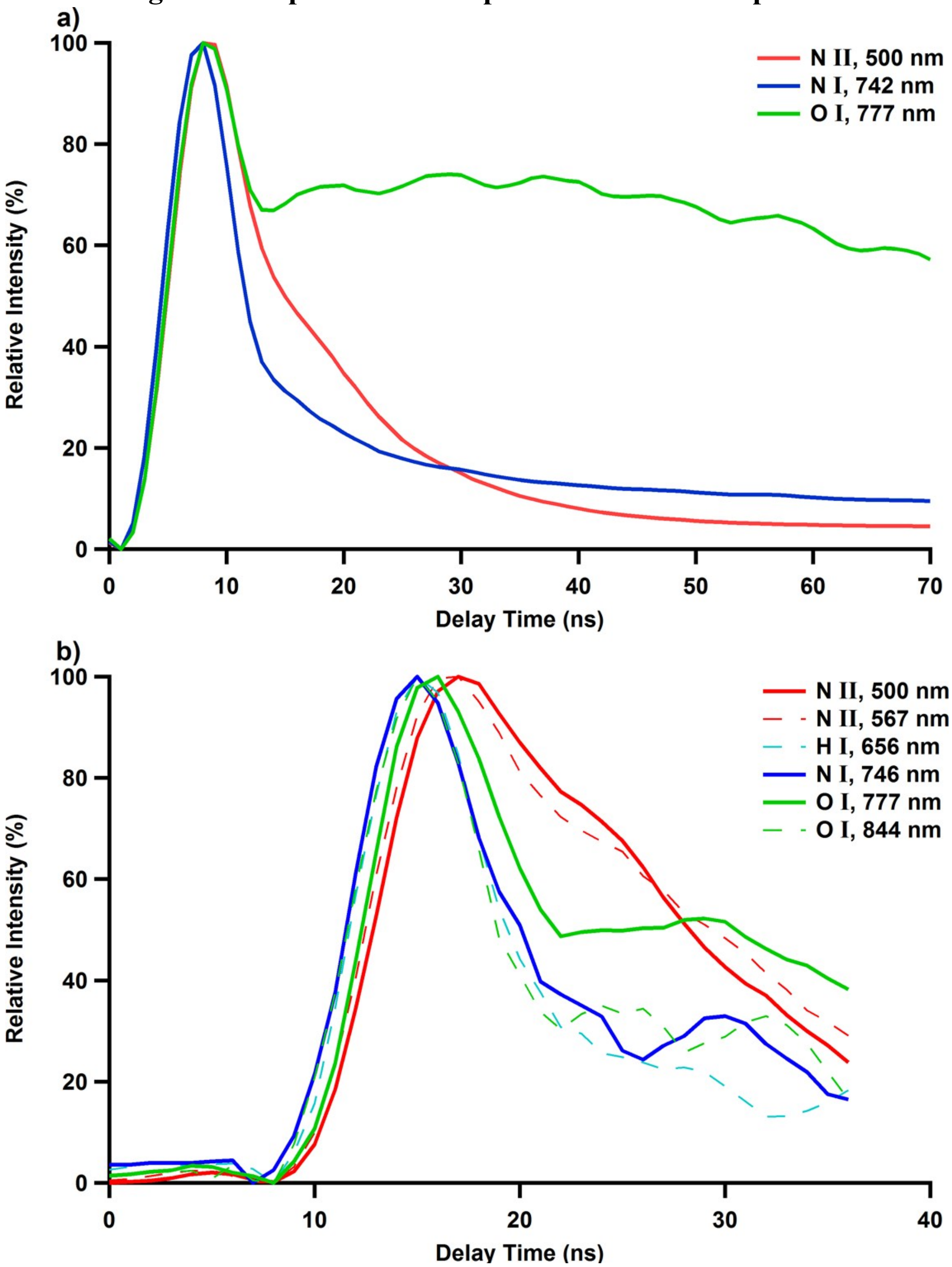

Figure S5. Temporal profiles of different species with two spectrometers. a) software-integrated temporal profile from the spectrograph. b) optically integrated temporal profile from Echelle spectrometer.

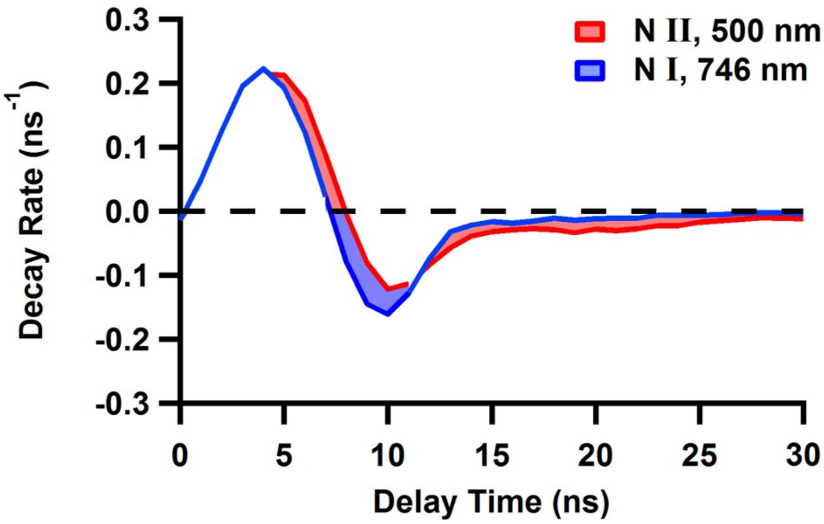

Figure S6. Decay rate of different species during the plasma lifecycle.

6. Excitation and ionization cross-section

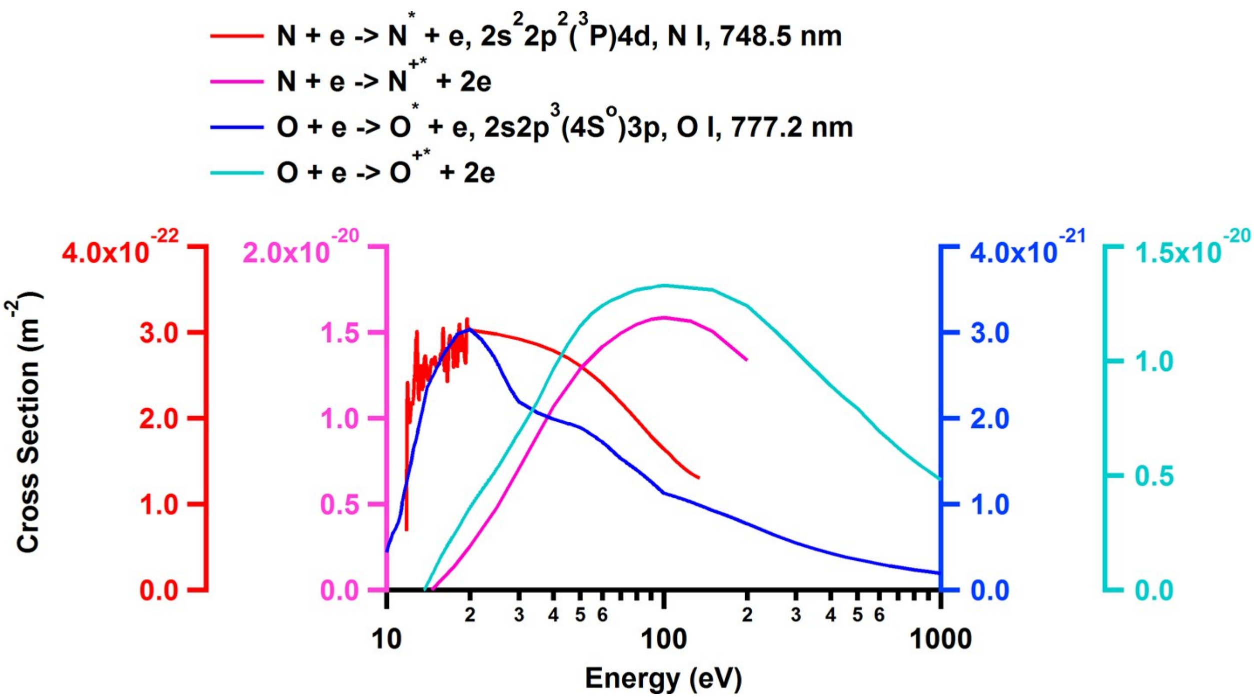

Figure S7. Electron-impact cross-secions of different species.

7. Adaptive moving average

The plasma trajectories (*cf.* Figure S8) was dynamically smoothed depending on the signal-to-noise ratio (SNR). With respect to the SNR, the minimal window size of averaging was set to 1, *i.e.* no smoothing, whereas that of the maximal was set to 13 (*cf.* Figure S8a). The window size of

1 was intentionally selected to preserve the feature at 7 ns, where the plasma travelled the furthest towards the source of the laser beam. Any greater window size will result in compromising this feature. In the later stage of the plasma, due to the low SNR and the digitizing error during determining the plasma center, the positions of the centers were perturbed significantly (*cf.* Figure S8c). In addition, the selection of the window sizes were empirically chosen. In specific, the window size of 13 data points were the greatest odd integer below 20% of the total number of data points, which is 72.

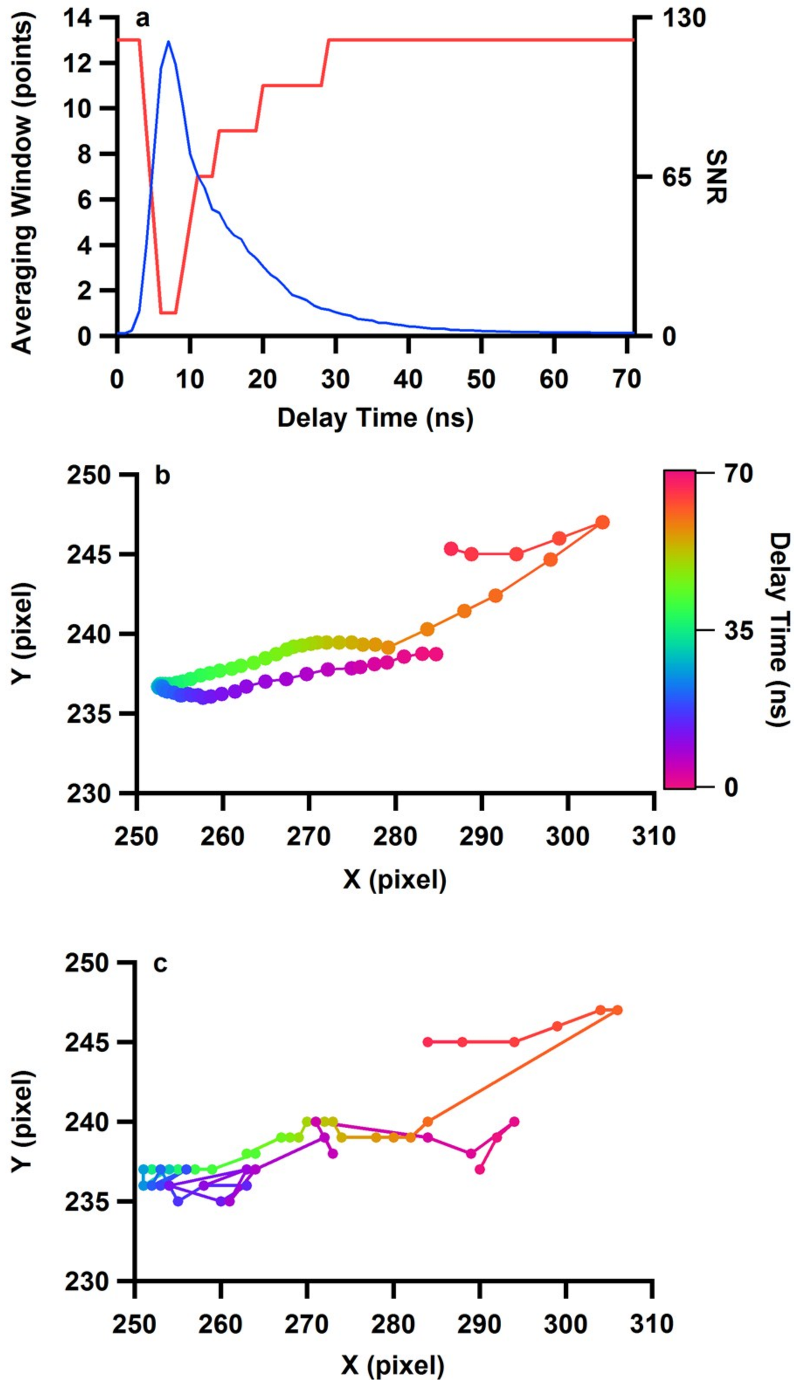

Figure S8. Adaptive smoothing for early-stage plasma evolution. a) adaptive window size of moving average. The blue and red traces are SNR and averaging window, respectively. b) and c) are the adaptively smoothed and raw trajectories of N II, respectively.

8. Transient profiles of additional points during the early stage of the plasma

Several different points were selected in addition to those of the plasma center. Roughly, they are selected along the path of the trajectory of the plasma center determined with overall-emission images. Notably, the blue and magenta points ()

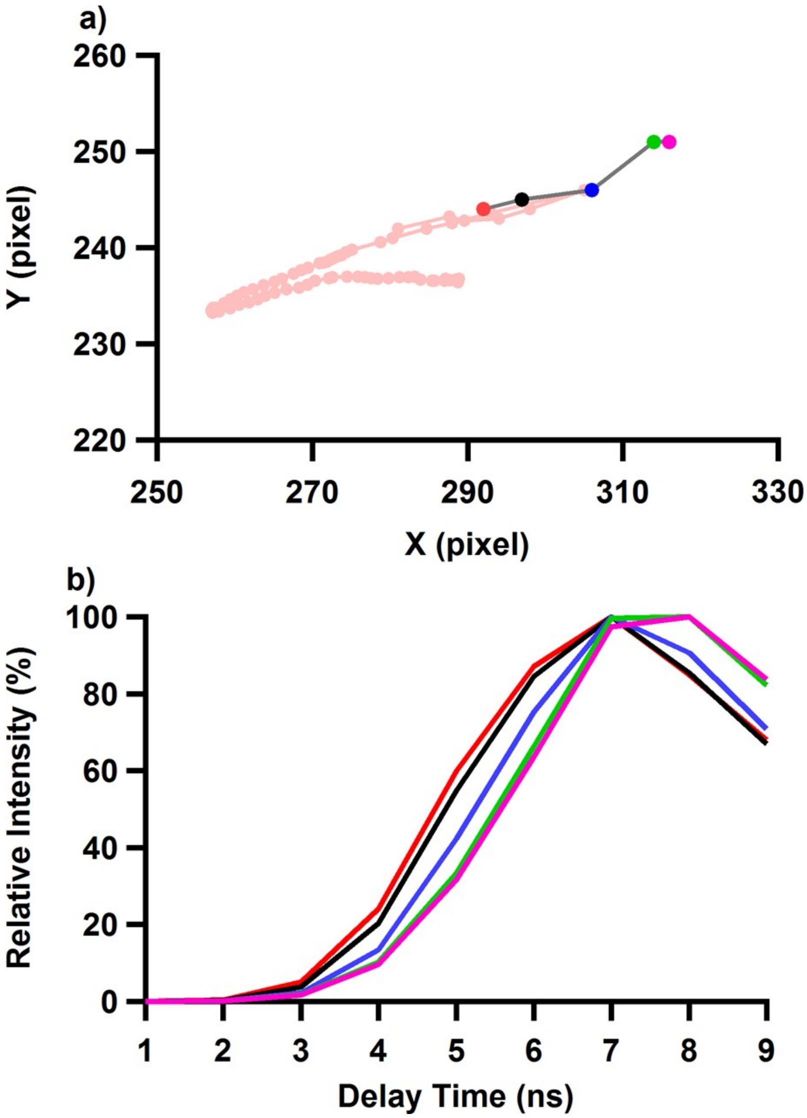

Figure S9. Transient profiles of additional points for the overall emission. The color of each line in b) corresponds to the points with the same color in a).

9. Determining the center of symmetry

Due to the asymmetries of the laser profile, which further induced the asymmetries in the intensity distribution particularly for the neutral excited species, the center of symmetry was later determined through the distribution of the decay rates (*cf.* Figure S10). We used elliptical profiles to describe the spatial distribution of the decay rate. Here, the spatial distribution of O I decay rates was used as a model.

The ellipse can be described as:

$$(x - x_c)^2 + F_o.^2 \cdot (y - y_c)^2 = R^2 \qquad \text{Eq.S1}$$

where x and y are the coordinates, x_c and y_c are the coordinates of the centers, F_o is the elliptical factor, and R is the radius. The decay rate between 0.02 ns^{-1} and 0.04 ns^{-1} were used as the thresholds to describe the decay distribution. Due to the higher decay rate on the left-hand-side of than that of the right-hand-side, we assigned a positive constant (*i.e.* 1) for those within the thresholds. The rest of the space were assigned with zeros. To optimize the factors in Eq.S1, a home-build global optimization method based on genetic algorithm was used. The details of this algorithm are beyond the scope of this work. Note that the global optimization can be performed with existing software platforms, such as Matlab.

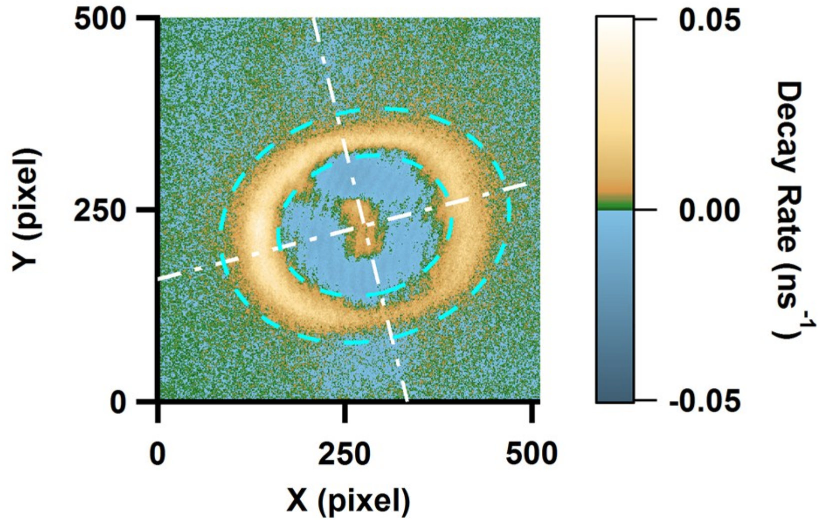

Figure S10. Determined center and axes of symmetry of O I (777 nm). The white center lines are the axes of symmetry, where the cross points is the center of symmetry. The cyan ellipses are the best fit of the decay rate distribution.

10. Spike removal

The recorded distributions of the emissions are commonly cluttered by hot pixels or cosmic rays. This case is particularly true for those with low intensities, *e.g.*, O I. Due to the low quantum efficiency of the camera in the red and near-IR region, the collection of O I signal requires a long exposure and maximal gain settings. The recorded image contained outliers that overwhelmed the true emission (*cf.* Figure S11a). In present work, a two-dimensional median filter with a window size of 7×7 was used to remove the spikes without significant compromise of the original feature (*cf.* Figure S11b).

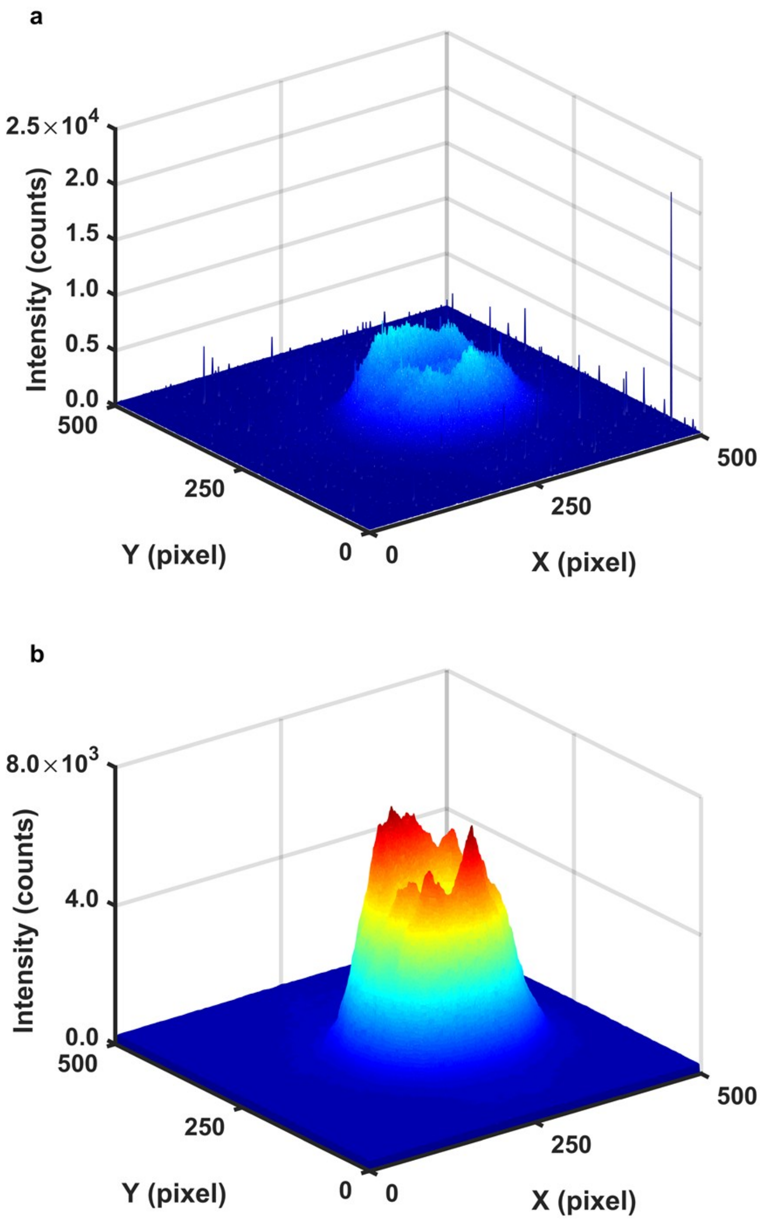

Figure S11. Spike removal. The distribution of O I (777 nm) at 15 ns without (a) and with (b) spike removal.

11. Smoothing

Throughout this study, the smoothing algorithms were needed for data in time domain or that in the space. For either cases, the raw data was convolved with a Gaussian profile through fast Fourier transform. The Gaussian profile can be described with:

$$K = e^{-\frac{(x-\mu)^2}{\sigma^2}} \qquad \text{Eq.S2}$$

where K is the Gaussian kernel function, x is the index, μ is the center of the Gaussian function, σ represents the width of the Gaussian peak. Then the raw data was convolved with this kernel function:

$$Y_{smth} = FT^{-1}[FT(Y) \circ FT(K)] \qquad \text{Eq.S3}$$

where Y_{smth} and Y are the smoothed and raw data, FT and FT^{-1} represent the Fourier transform and inverse Fourier transform, K is the kernel function, and the ◦ is the Hadamard multiplication of matrices/vectors.

To improve the computational efficiency, radix-2 Fourier transform was used. Thus, for raw data that has a length smaller than 512 were zero-filled to such a length. Meanwhile, the μ and σ^2 were selected as 255 and 10.

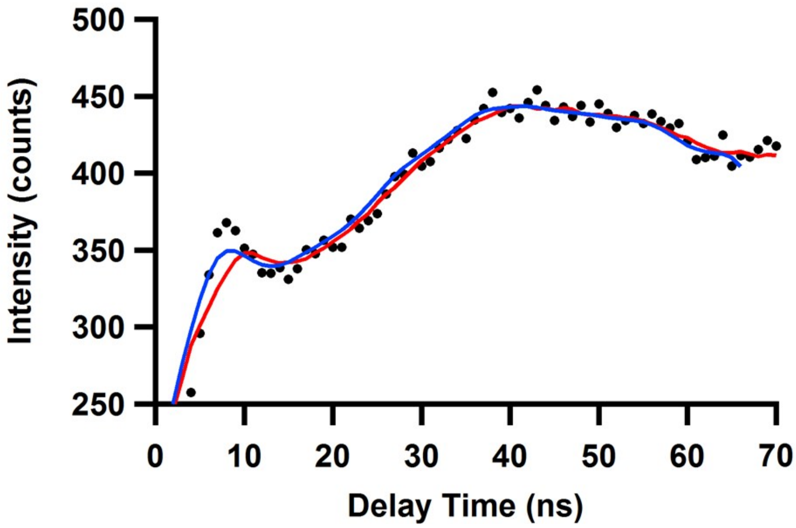

Figure S12. Comparison of the smoothing approaches. The black dots are the temporally resolved emission intensity at 777 nm of coordinate (118, 189). The red and blue traces are boxcar and Gaussian convolution smoothing algorithms, respectively.

As an example, one of the time-domain profiles of the O I at coordinate (118, 189) was used to demonstrate the advantage of using Gaussian-based smoothing over boxcar smoothing (*cf.* Figure S12). The result of smoothing commonly suffer from broadening and shifting of the features in the original data. For instance, the boxcar smoothing significantly shifted the peak feature of the raw time-domain profile by 2 ns (*cf.* Figure S12, red trace). In contrast, the Gaussian-based approach preserved such features.

In cases of image smoothing, *e.g.*, the smoothing of the vector, two-dimensional (2D) convolution was used:

$$Y_{smth} = FT_{2D}^{-1}[FT_{2D}(Y) \circ FT_{2D}(|K\rangle\langle K|)] \qquad \text{Eq.S4}$$

where FT_{2D} represents the 2D Fourier transform, the outer product of the Gaussian kernel denotes the matrix containing a 2D Gaussian peak at center.

12. Determine the movement velocities with different approaches

The movement velocity can be determined through gauging the local maxima the time-domain profiles correspond to each pixel. To demonstrate this approach, the O(I) was used as an example due to the rich features throughout the image. The time-domain profiles at different pixel points exhibited distinctive features (*cf.* Figure S13b). As an example, the point corresponding to the red arrow reached the maximum after that of the black arrow (*cf.* Figure S13a). A continuous motion was observed from the starting point (black arrow) to the end point (red arrow). Thus, the delay times corresponding to that when the time-domain profiles reached the maximum after 15 ns (t_{max}) were plotted (*cf.* Figure S13a).

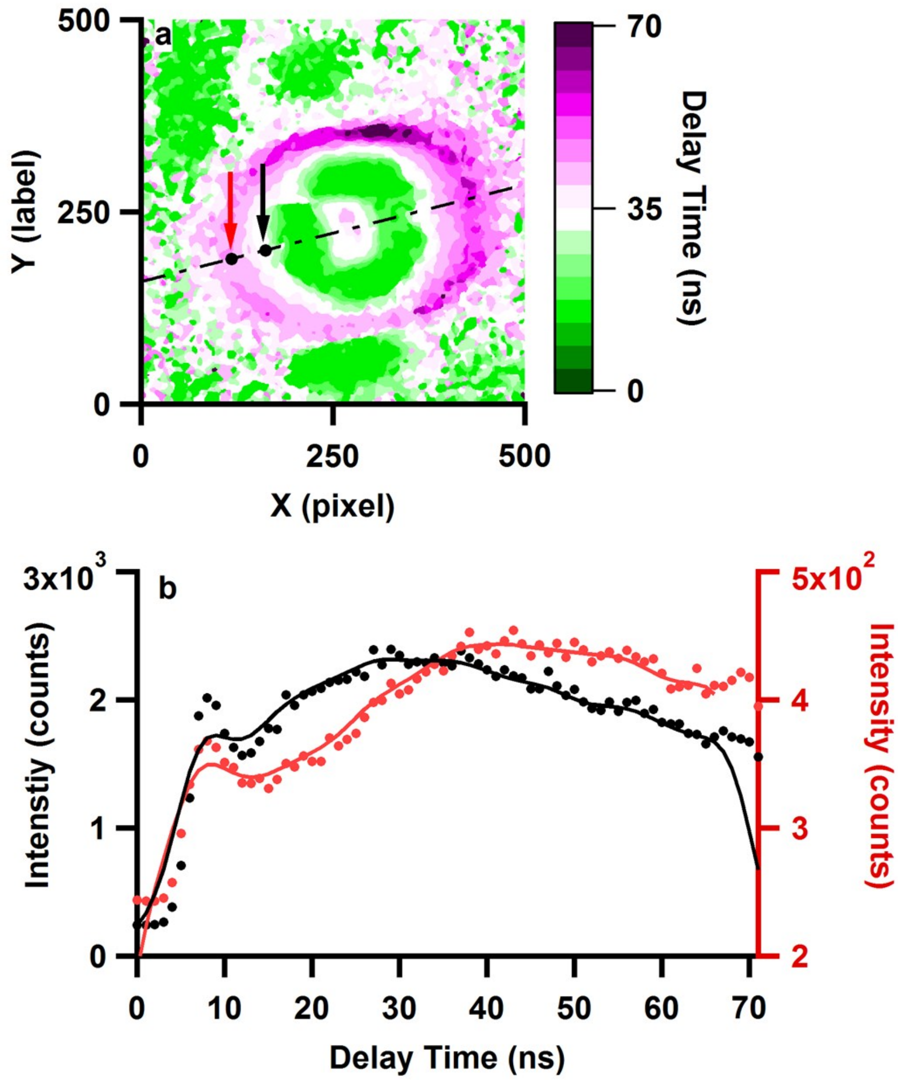

Figure S13. O(I) movement velocity determination through time delay. a) shows the pseudo color plot of the regional maximum of each pixel. b) represents the time-domain profiles of points corresponds to the red and black arrows in a).

The velocity field of O(I) species was then calculated based on the gradient t_{max}:

$$\vec{\nabla} t_{max} = \begin{bmatrix} \frac{\partial}{\partial x} t_{max} \cdot \hat{i} \\ \frac{\partial}{\partial y} t_{max} \cdot \hat{j} \end{bmatrix} \qquad \text{Eq.S5}$$

$$\vec{V} = \frac{1}{\vec{\nabla} t_{max}} \qquad \text{Eq.S6}$$

Due to the limited steps of delay time, *i.e.* 1 ns, the determined t_{max} values were cluttered because of the digitizing error (*cf.* Figure S14). Thus, the time-domain profiles of each pixel were linearly interpolated and the smoothed prior to determining the local maxima. The data density was increased by 5-fold after interpolating with a time step of 20 ps. Consecutively, the Gaussian-convolution-based smoothing with a window size of 50 was used to smooth the convolved data. In terms of delay time, the smoothing window always covered 10 ns region.

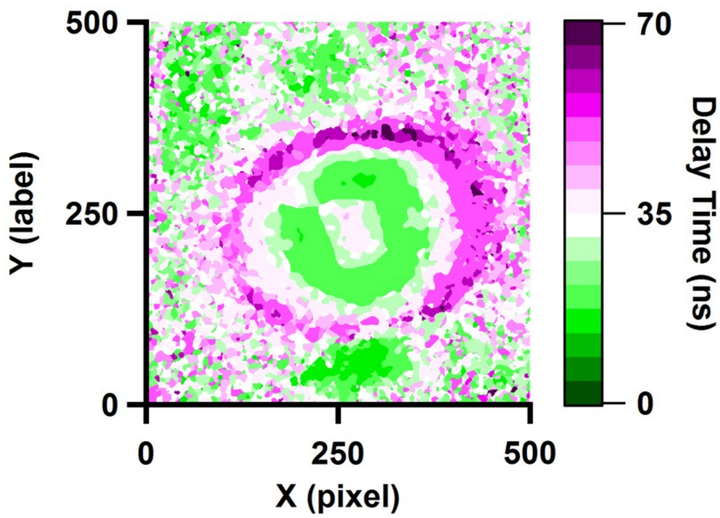

Figure S14. T_{max} of O(I) without data interpolation.

The determined velocity field from the t_{max} approach (*cf.* Figure S15b) showed highly similar features comparing to that of the optical flow approach (*cf.* Figure S15a). Specifically, the expansion and retraction features were observed in both cases. However, the determined values of the movement speed are quite different from each other. Essentially, the movement interpretation from the t_{max} approach utilized only one data point per pixel by obtaining the delay time corresponds to the maximal intensity. Thus, the error inherited from neglecting the rest of the data points might be the reason for such high velocities comparing to that obtained with optical flow approach, which utilized all information from the 4-D space, *i.e.* x, y, time, and intensity. As such, in present study, the movement of the plasma was gauged with optical flow approach.

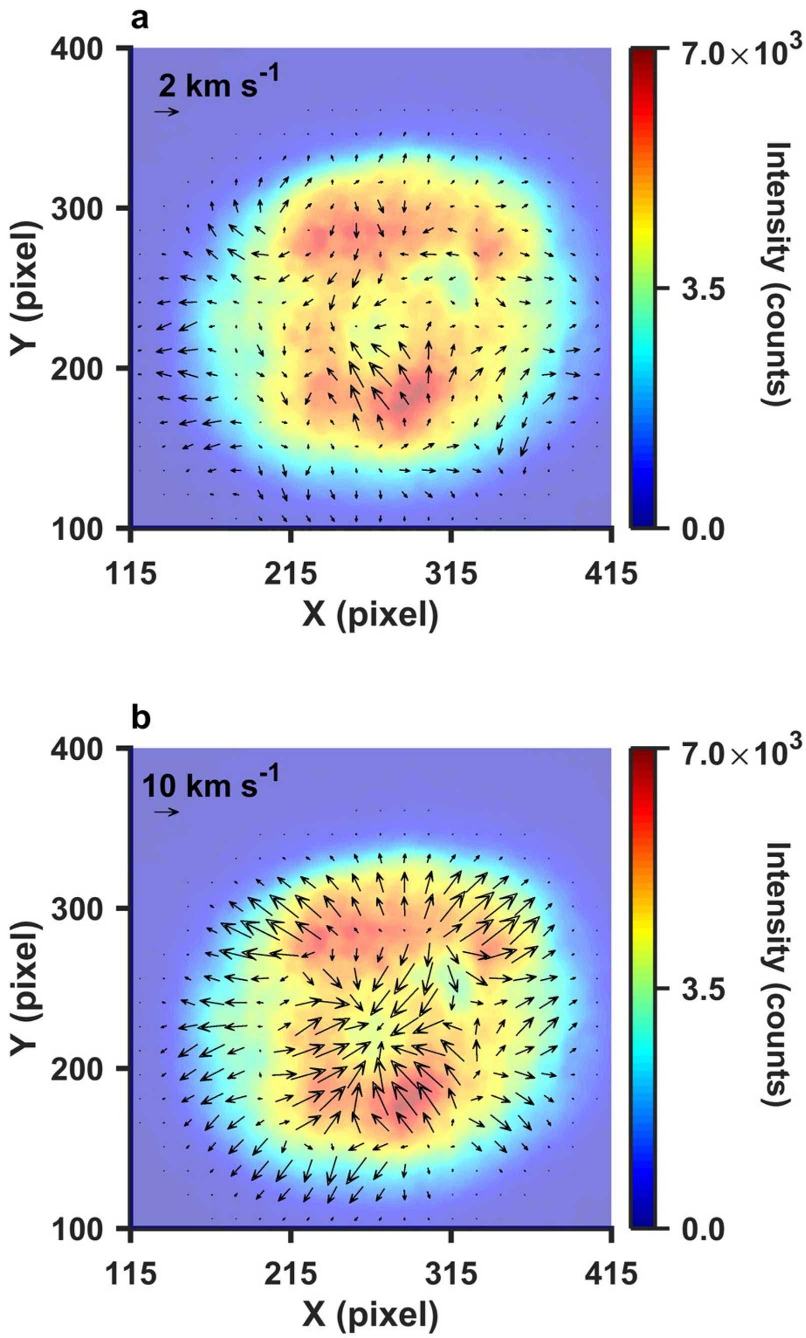

Figure S15. Velocity fields of O(I) migration with a) optical flow approach, and b) with t_{max} method.